Ni Mg mixed metal oxides for p-type dye-sensitized solar cells.

Marco Zannotti[§,‡], Christopher J. Wood[§†], Gareth H. Summers[§†], Lee A. Stevens[ǂ], Matthew R. Hall[ǂ], Colin E. Snape[¥], Rita Giovannetti[‡], and Elizabeth A. Gibson[§†]*

§ School of Chemistry, University of Nottingham, University Park, Nottingham, NG7 2RD, UK

† School of Chemistry, Newcastle University, Newcastle upon Tyne, NE1 7RU, UK

‡ Chemistry Unit, School of Science and Technology, University of Camerino (MC), Via S.Agostino 1, 62032, Italy

ǂ Division of Materials, Mechanics and Structures, Faculty of Engineering, University of Nottingham, University Park, Nottingham, NG7 2RD, UK

¥ Department of Chemical and Environmental Engineering, Faculty of Engineering, University of Nottingham, University Park, Nottingham, NG7 2RD, UK

KEYWORDS dye-sensitized solar cells, nickel oxide, p-type, photocathode, artificial photosynthesis

Abstract

Mg Ni mixed metal oxide photocathodes have been prepared by a mixed $NiCl_2/MgCl_2$ sol-gel process. The MgO/NiO electrodes have been extensively characterized using physical and electrochemical methods. Dye-sensitized solar cells have been prepared from these films and the higher concentrations of MgO improved the photovoltage of these devices, however, there was a notable drop in photocurrent with increasing Mg^{2+}. Charge extraction and XPS experiments revealed that the cause of this was a positive shift in the energy of the valence band which decreased the driving force for electron transfer from the NiO film to the dye and therefore the photocurrent. In addition, increasing concentrations of MgO increases the volume of pores between 0.500 to 0.050 μm, while reducing pore volumes in the mesopore range (less than 0.050 μm) and lowering BET surface area from approximately 41 down to 30 $m^2\ g^{-1}$. A MgO concentration of 5% was found to strike a balance between the increased photovoltage and decreased photocurrent, possessing a BET surface area of 35 $m^2\ g^{-1}$ and a large pore volume in both the meso and macropore range, which lead to a higher overall power conversion efficiency than NiO alone.

Introduction

The dye-sensitized solar cell (DSC) is a low cost alternative to crystalline silicon photovoltaics that converts sunlight into electricity using a dye adsorbed on a transparent, nanostructured semiconductor electrode, surrounded by a redox electrolyte. Almost all of the current research in dye-sensitized solar cells is focused on n-type systems, typically based on TiO_2. Unlike the standard DSC, which has a passive counter electrode, tandem devices simultaneously use two

photoelectrodes to harvest a greater proportion of the solar spectrum more efficiently. Incorporation of a photocathode in tandem with a TiO_2-based n-type photoanode in a single device should give rise to a substantial increase in voltage and efficiency. By choosing sensitizers which absorb the high energy photons on one electrode and low energy photons on the other, more of the solar spectrum can be utilized. Tandem DSCs have not yet beaten the best n-type DSCs because the poor performance of dye-sensitized photocathodes limits the overall efficiency.

One of the main reasons for the low efficiency of p-DSCs is the low photovoltage. When light is absorbed by the dye in a p-DSC, an electron is extracted from the valence band of the p-type semiconductor (NiO) and transferred to the photoexcited dye and the excited electron in the dye is transferred to the redox electrolyte (I_3^-). The photovoltage is the potential energy difference between the quasi-Fermi level close to the valence band in NiO and the redox potential of the I_3^-/I^- electrolyte. Since the position of the valence band is close to the redox potential of the electrolyte, the built in voltage of the device is small. Improvements to the voltage have been made by tuning the crystallinity of the material[1], depositing an insulating layer of Al_2O_3 on the surface of NiO[2] and exchanging the redox couple for cobalt coordination complexes.[3] Recently, there have been a number of papers reporting improvements to the efficiency of p-DSCs by doping the semiconductor. D'Amario *et al*.[4] doped NiO with Li and Natu[5] doped NiO with Co to improve the V_{OC}, whereas Renaud[6] *et al.* and Xiong[7] doped $CuGaO_2$ and $CuCrO_2$ respectively with Mg to improve the short-circuit photocurrent density(J_{SC}).

This article describes the effects of adding Mg^{2+} to NiO on the performance of p-DSCs. Solid solutions of MgO and NiO can easily be made because Mg^{2+} and Ni^{2+} have similar ionic radii and both favor a rock-salt structure with a similar lattice constant. MgO has a much wider band gap than NiO (E_g MgO = 7.8 eV[8], E_g NiO = 5.4 eV[9]). Various amounts of Mg^{2+} were added to the sol-

gel NiO precursor solution from 1% to 25% Mg:Ni by weight. We have found a similar relationship between the Mg:Ni ratio and the device performance to Huang *et al.* who recently published a similar study.[10] This article provides details on the physical and electrochemical properties of the films, such as the porosity of the material and the surface composition, as well as solar cell characteristics. The efficiency of the solar cells was slightly improved in this study and we are now able to provide further explanation of the trends observed in p-DSCs as the Mg content is varied.

Materials and Methods

p-Type Dye Sensitized Solar Cells

NiO working electrodes were prepared using the sol-gel method described by Sumikura *et al*.[11,12] Precursor solutions were prepared by dissolving $NiCl_2$ (1 g) and the triblock co-polymer F-108 (1 g) in a mixture of ultra-pure water (3 g) and EtOH (6 g). The NiO precursor solutions were prepared with different amounts of $MgCl_2$ (1, 5, 10, 25 *wt.* %).

All solutions were stirred for 1 night, and were used after 2 days. NiO films were prepared by applying thin films of the precursor onto conducting FTO (SnO_2:F) glass substrates (Pilkington TEC15, sheet resistance 15 Ω/square) by doctor-blade using Scotch tape as a spacer (0.2 cm^2 active area) in 3 cycles, annealing in a furnace in air at 450 °C for 30 minutes between layers. The NiO electrodes were soaked in an acetonitrile solution of the dye (0.3 mM) for 16 hours at room temperature. The dyed NiO electrodes were assembled face-to-face with platinized counter electrodes (Pilkington TEC8, sheet resistance 8 Ω/square) using a 30 μm thick thermoplastic frame (Surlyn 1702, Dyesol). The electrolyte, containing LiI (1.0 M) and I_2 (0.1 M) in acetonitrile, was

introduced through the pre-drilled hole in the counter electrode, which was sealed afterwards. The UV-visible absorption spectra of the dyes adsorbed on NiO films were recorded using a USB2000+VIS-NIR Ocean Optics fiber optic spectrophotometer. The concentration of dye adsorbed onto each film was calculated by the difference in the absorption spectra of the dye solution before and after immersing the film, using ε_{480} = 58000 M^{-1} cm^{-1}. Current-voltage measurements were measured using an Ivium CompactStat under simulated sunlight from an Oriel 150 W solar simulator, giving light with an intensity of 100 mW cm^{-2}. Incident photon-to-current conversion efficiencies were recorded using light from the solar simulator passed through a Cornerstone monochromator and calibrated against a certified reference Si photodiode. Impedance spectra and hole transport times and lifetimes in the complete devices were measured using time-resolved small light modulation techniques using an Ivium CompactStat fitted with a Modulight.[13]

Transmission Electron Microscopy

NiO and 5% *wt.* MgO/NiO samples were prepared as described above. The NiO and MgO/NiO was removed from the FTO glass and loaded onto a carbon coated copper TEM grid (Agar Scientific). A JEOL 2100F TEM equipped with a JEOL digital STEM system and a Gatan Tridiem spectrometer was used for the TEM experiments. EDX/EELS spectra were taken using Oxford Instruments INCA TEM 250 X Ray Microanalysis system. Particle sizes were obtained from the TEM images using ImageJ software (National Institutes of Health, Bethesda). Average particle sizes were taken from the mean of the long and short lengths of 24 (NiO) and 16 (MgO/NiO) clearly visible particles. For the MgO/NiO sample particles larger than 40 nm were excluded from the average particle size. EDX and EELS data were fitted to the reference data using Origin Pro 8.0.[14]

Gas Adsorption Isotherms

Gas adsorption isotherms were carried out by using a Micromeritics ASAP 2420, using krypton as the adsorbate. MgO/NiO samples were prepared as described above onto ~ 0.5 cm × 1.0 cm FTO glass substrates. Three replicates of each sample were inserted into glass sample tubes with a sealed frit. The samples were degassed under high vacuum (0.0002 psi) at 25 °C for 3 hours to remove moisture and other adsorbed gases. Krypton isotherms were acquired from 0.07-0.20 relative pressure (P/P_o) at -195.85 °C in liquid nitrogen. The replicate samples were then weighed and reweighed following the removal of the MgO/NiO in order to give an accurate sample weight associated with the MgO/NiO layers. Specific surface area of the samples were determined by using the standard BET method over the isotherm range. An isotherm was also acquired on a blank FTO glass substrate to show adsorption was associated with the MgO/NiO layers.

Mercury Intrusion Porosimetry

Mercury intrusion porosimetry (MIP) was carried out on the MgO/NiO samples using a Micromeritics Autopore IV 9505.V1. The instrument has a maximum pressure of 60,000 psi allowing pores from 390-0.003 μm to be analyzed. MgO/NiO samples were prepared as described above onto 0.5 cm × 1.0 cm FTO glass substrates. Three replicates of each sample were inserted into a solid penetrometer (0.37 cm internal stem diameter). The samples were degassed under high vacuum (0.0002 psi) at room temperature for 60 minutes to remove any moisture and both low and high pressure analysis were carried out from 0.5-60,000 psi with an equilibration time of 45 seconds per pressure point. Surface tension and contact angles were taken as 0.485 N m^{-2} and 140° respectively. A blank correction was carried out prior to analysis and intrusion subtracted from the sample data. Textural properties such as total pore/intrusion volume, average pore and size distribution can be calculated from intrusion data. Accurate average pore diameters can be determined by removing the weight associated with the FTO glass substrate, as described above.

Inductively Coupled Plasma Optical Emission Spectroscopy

NiO and MgO/NiO samples were prepared as described above onto ~ 0.5 cm x 1.0 cm FTO glass substrates. The MgO/NiO samples were then removed from the FTO glass. Prior to ICP-OES measurements, a 4-6 mg sample of material was digested in Aristar grade nitric acid (69 %) for 24 hrs. The sample was then filtered using a syringe filter and diluted to the required concentration using Milli-Q ultrapure water. ICP-OES was performed using a Perkin-Elma Optima 2000.

X-Ray Diffraction

Powder X-ray diffraction (PXRD) data was collected on a PANanalytical Multi-purpose Diffractometer operated at 40 kV and 40 mA (Cu Kα1, λ= 1.5406 Å) for MgO/NiO films on FTO (prepared as described previously) and on a silicon zero diffraction plate. The data was analysed using PANanalytical X'Pert Highscore.

X-ray photoelectron spectroscopy

X-ray photoelectron spectroscopy (XPS) was carried out using a Thermo Scientific K-Alpha X-Ray Photoelectron Spectrometer with an Al K_α X-ray source (1486.7 eV) on thin film MgO/NiO samples on FTO. For binding energy calibration, the C 1s peak (resulting from adventitious surface carbon) was referenced to a binding energy of 284.8 eV. CasaXPS was used for all data analysis and fitting.

Electrochemistry

Cyclic voltammetry was carried out using a Palmsens Emstat potentiostat. A three electrode system was used with the NiO film working electrode, Pt wire counter electrode and a Ag/Ag^+ (0.01 M $AgNO_3$ in acetonitrile) reference electrode. The supporting electrolyte was 0.1 M Bu_4NClO_4 or $LiClO_4$ in acetonitrile. The potentials were calibrated against a $Fe(Cp)_2^{+/0}$ external standard.

Electrochemical Impedance Spectroscopy

Impedance spectroscopy was carried out on two electrode devices prepared in the same way as for the p-DSCs, with the electrolyte used consisting of 0.1 M $LiClO_4$, 0.1 M LiI and 0.1 M I_2 in acetonitrile. Different bias potentials were applied (from 0 to 900 mV) and scanning frequencies between 10 KHz and 100 mHz with an amplitude of 10 mV.

Dye Loading

Dye bath solutions of P1 (2.8×10^{-4} M) were prepared in dry CH_3CN. The NiO and 1-20 % *wt.* MgO/NiO electrodes were prepared as described above. The films were immersed in P1 dye baths and the UV-visible absorption spectra of the films were monitored at regular time intervals. The UV-visible absorption of the sensitized MgO/NiO films were recorded on a Hewlett-Packard 8452A diode array spectrophotometer; to remove the interference, the absorbance was monitored after subtracting the spectrum of the MgO/NiO film.

Results

Characterisation of NiO with different amounts of MgO

Composition and physical properties

Table 1. Summary of the physical properties of NiO electrodes with different amounts of MgO.

% wt. $MgCl_2$[a)]	% mol. Mg^{2+}	Crystallite size [nm][b)]	BET surface area [$m^2\ g^{-1}$]	Total intrusion volume [$cm^3\ g^{-1}$][c)]	Average pore diameter (4V/A) [µm][d)]	Dye adsorption [µmol cm^{-3}]
0	0	20	40.6 ± 0.8	2.16	0.213	4.59
1	1.67	21	43.3 ± 0.2	1.58	0.147	5.21
5	7.34	20	35.3 ± 0.4	1.12	0.127	6.48

10	14.3	22	28.0 ± 0.03	3.84	0.547	7.42
25	34.3	19	29.9 ± 0.06	4.04	0.540	8.74 (20%)

a) % *wt.* $MgCl_2$ added to NiO precursor solution; b) average determined from pXRD pattern; c) from MIP from 6 – 0.003 μm, and subtracting glass weight. d) average pore diameter using total intrusion volume (V) and BET specific surface area (A).

Powder X-ray diffraction

p-XRD reveals that cubic NiO (bunsenite) is formed in all samples, see Figures S8-12 in the ESI. Cubic MgO has a similar diffraction pattern to cubic NiO and we did not observe any new features in the diffraction patterns for MgO/NiO, nor any significant differences in the full width half maximum (FWHM) for the peaks. From the peak broadening, an average NiO crystallite size of 20±1 nm was calculated using the Scherrer equation which is slightly larger than observed by Sumikura *et al.* (12 nm) and Li *et al.* (16 nm) for NiO prepared using similar methods. The crystal sizes for the MgO/NiO samples are listed in Table 1 and are consistent with the NiO only sample within 2 nm. This suggests that the crystal size of the NiO was not affected by mixing with MgO. Huang *et al.* reported a crystallite size of 10-15 nm for their MgO/NiO samples.[10] We attribute the difference to the larger quantity of water in the sol-gel precursor in their preparation compared to those used in this study.

Transmission electron microscopy

Figure 1 shows TEM images of NiO nanoparticles and 5% *wt.* MgO/NiO. The clearly defined polycrystalline diffraction patterns (a,d) demonstrate that both the NiO and 5 % *wt.* MgO/NiO are highly crystalline. The 400,000 × magnified images show the particle size to be 14±3 nm for NiO and 21±10 nm for 5% *wt.* MgO/NiO which is in general agreement with the crystallite sizes determined by p-XRD (above). The 5% MgO/NiO sample gave a far broader range of particle

sizes and overall the particle size was slightly larger (19.6 ± 9 nm). In addition to the primary particles there were a small number of significantly larger particles visible (40-55 nm) indicating sintering and agglomeration of the particles in the furnace. Figure 2 shows the energy-dispersive X-ray spectra (EDX) of 5% *wt.* MgO/NiO. From this data, a Mg:Ni ratio of 0.0717: 1 was calculated, which compares extremely well to the calculated molar ratio for the addition of 5% *wt.* $MgCl_2$ to the precursor solutions (Table 1). The C and Cu peaks arise from the carbon coated copper grids. Also shown in Figure 2 is a dark field STEM image and EDX elemental maps of the same sample, which indicate that the distribution of Ni, Mg and O is consistent throughout the 5% MgO sample.

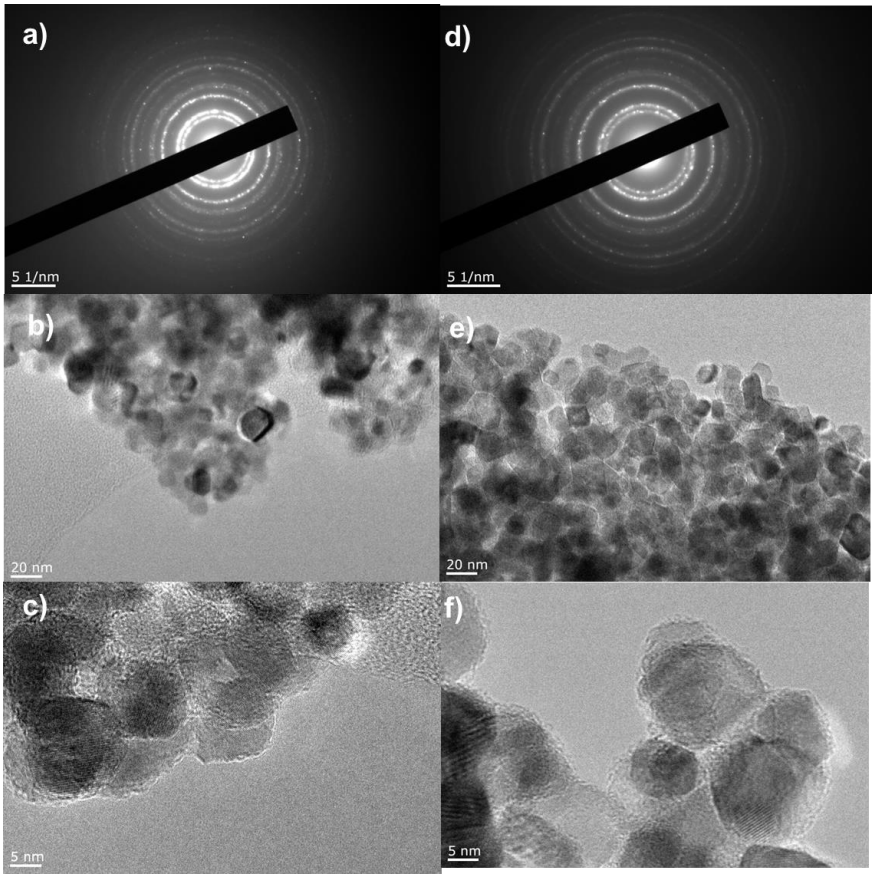

Figure 1. TEM images and diffraction patterns (a, d) for NiO (a-c) and MgO/NiO (d-f) at 100 000 × magnification (b,e) and 400 000 × magnification (c,f).

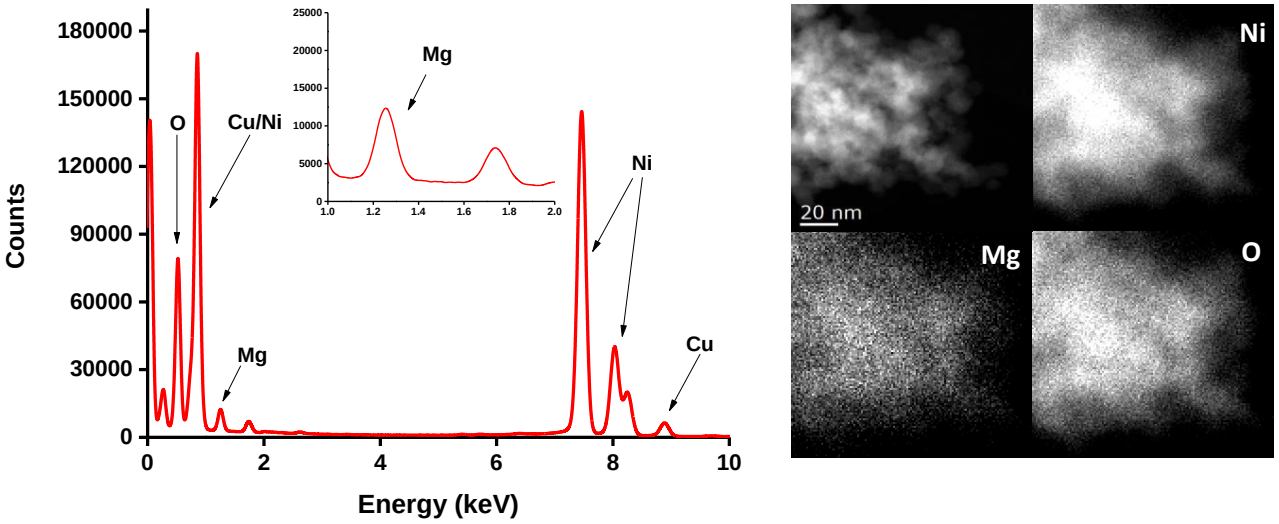

Figure 2. Left: EDX spectra of 5 % wt. MgO/NiO; Right: Dark Field STEM image and EDX maps measured using EELS of 5 % wt. MgO/NiO, demonstrating an even dispersion of MgO throughout the sample.

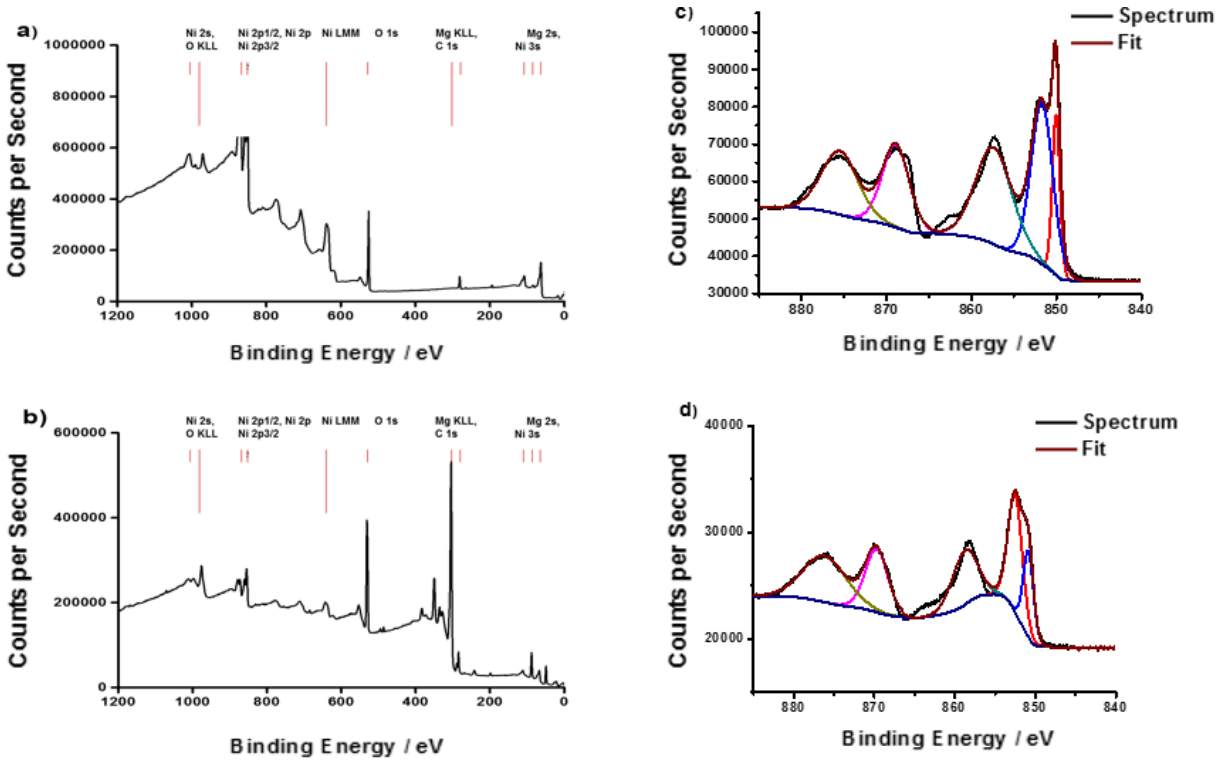

Figure 3: a) XPS spectrum, NiO, b) XPS spectrum, MgO/NiO (25%), c) Ni2p XPS spectrum, NiO, d) Ni2p XPS spectrum, MgO/NiO (25%).

Table 2: Summary of XPS results.

Sample	Ni $2p_{3/2}$ / eV	Ni $2p_{1/2}$ / eV	O 1s / eV	Mg 2s / eV	O defects %	Ni^{3+} %
0%	853.3, 855.9, 860.7	870.8, 879.9	529.1, 531.1	-	30.13	42.5
1%	853.3, 855.8, 860.8	870.9, 879.6	529.1, 530.9	87.9	29.68	41.4
5%	853.3, 855.8, 860.8	870.9, 880.1	529.0, 531.0	87.5	31.84	40.6
10%	852.7, 855.3, 860.1	870.9,878.1	528.4, 530.5	87.1	38.48	45.4
25%	855.5, 861.1	870.9, 878.8	529.4, 532.1	88.2	59.82	48.4

XPS analysis (Figure 3 and S13) confirms the presence of MgO within the NiO samples from the characteristic peaks at 87 (Mg 2s) and 306 (Mg KLL auger line) eV (Table 2). The position of the peaks for the samples of increasing Mg content are very similar and within experimental error. A small feature is seen at a binding energy of 87 eV for the NiO-only sample (Figure S16a), however due to the lack of the more intense KLL line this has not been assigned as Mg. The Ni 2p peak can be deconvolved into five distinct peaks; three at lower binding energies assigned to the Ni $2p_{3/2}$ peaks and two at higher energies assigned to the Ni $2p_{1/2}$ peaks. The peak at 855.9 eV has been previously attributed to surface Ni^{3+} species[15] and so comparing the ratio of this peak with the total Ni $2p_{3/2}$ peak will give an approximate ratio of Ni^{3+}:Ni^{2+}, which increases from 42.5% Ni^{3+} for NiO to 48.4% for MgO/NiO (25%). A similar comparison of the shoulder peak in the O 1s spectra (Figure S15), which has been attributed to oxygen defect sites, shows an increase in the amount of defect sites from 30.13 % for NiO to 59.82% for MgO/NiO (25%). Valence band measurements (Figure S17) show a positive shift from 0.375 eV for NiO to 0.411 and 0.432 eV for 5% and 25% MgO/NiO respectively.

Textural properties

The Kr adsorption isotherms data (Figure S5) show zero adsorption on the plain FTO glass, with adsorption occurring on the NiO and MgO/NiO films. Therefore, the weight of the glass can be removed as adsorption is exclusively due to the oxide layers on the glass surface. BET surface areas are summarized in Table 1. The NiO sample has a specific surface area of 40.6 $m^2 g^{-1}$, which is in agreement with Sumikura *et al.* (43.6 $m^2 g^{-1}$). The 1% *wt*. MgO sample shows similar adsorption to the NiO sample (maximum adsorption of 9.45 and 8.74 $cm^3 g^{-1}$) with comparable surface areas (43.3 and 40.6 $m^2 g^{-1}$ respectively). Further doping leads to a decrease in adsorption of Kr (6.63 $cm^3 g^{-1}$ for 25% *wt*. MgO/NiO) resulting in a drop of specific surface area from approximately 40 to 30 $m^2 g^{-1}$.

MIP shows large pore volume for pores between approximately 390 to 6 μm throat diameter, which are associated with voids and imperfections on the plain FTO glass (Figure S5). The plain glass has the largest pore volume within this range at 0.0044 $cm^3 g^{-1}$. This was expected as subsequent layers will block the entries to these voids and so reduce total intrusion. The plain FTO glass has zero intrusion below 6 μm throat diameter, indicating that the glass has no detectable pores at smaller pore sizes, therefore any intrusion less than 6 μm will be due to NiO and MgO/NiO layers. Therefore, the weight from the glass can be removed giving accurate intrusion or pore volume associated with the MgO/NiO layers. Figure S5 shows a thorough characterization of pores between 6 – 0.003 μm on the MgO/NiO layers.

Increasing the MgO concentration appears to decrease the pore volume in the mesopore range (less than 0.050 μm) while increasing pore volume in the macropore range (greater than 0.050 μm), specifically between 0.500 to 0.050 μm (Table 3), reducing BET surface area. Both 10 and 25% MgO/NiO samples show an increase in pore volume to 3.84 and 4.04 $cm^3 g^{-1}$ within this macropore range, with zero percentage of mesopores. However, a Mg concentration of 5% is at the threshold

where mesopores begin to disappear or become enveloped by macropores. Table 3 suggests that concentrations between 10 – 20 % have the greatest effect on pore size distribution.

Table 3. Intrusion or pore volume per pore size range from cumulative intrusion by MIP.

% *wt.* $MgCl_2$	1.500 – 0.500 [$cm^3 g^{-1}$]	0.500 – 0.150 [$cm^3 g^{-1}$]	0.150– 0.050 [$cm^3 g^{-1}$]	0.050– 0.025 [$cm^3 g^{-1}$]	0.025 – 0.010 [$cm^3 g^{-1}$]	0.010 – 0.003 [$cm^3 g^{-1}$]	% meso-porosity
0	0	0	0	1.21	0.95	0	100
1	0.09	0.33	0.42	0.58	0.04	0.12	47
5	0.13	0.26	0.51	0	0.15	0.08	21
10	1.4	0.55	1.89	0	0	0	0
25	0	1.53	2.51	0	0	0	0

Electrochemical Properties

Cyclic voltammetry was used to characterize the electrochemical properties of the MgO/NiO electrodes in acetonitrile (the solvent used for the electrolytes of the p-DSCs) and the data is presented in Figure 4. In each voltammogram a broad cathodic and anodic peak are visible and the beginning of a second process. This is in agreement with previous data from Boschloo *et al*.[16] and Awais *et al.*[17] for NiO prepared by different means. The peak currents scale linearly with the scan rate, also in agreement with Boschloo *et al.* which is consistent with the occurrence of surface redox reactions such as the oxidation of Ni^{II} to Ni^{III} coupled with cation desorption.[16] The peak currents are within 50 μA for each sample suggesting that the electroactive area is unchanged by the amount of Mg present. The slope of the peak is also similar for each sample indicating that there is little difference in resistance for this redox process regardless of the different amounts of MgO present in the electrode. The peak separation was generally similar for all samples and increased with increasing scan rate. Boschloo *et al.* attributed this to uncompensated resistance in

the cell due to the surface-mediated hole transport.[16] The average of the peak maxima shifted from –268 mV for NiO to more positive values with increasing concentration of MgO reaching +33 mV for 25% *wt.* MgO/NiO. This is consistent with the positive shift in the flat-band potential observed by Huang *et al.*[10] Interestingly, our results suggest that even though MgO is an insulator, the conductivity was not substantially decreased for 25% *wt.* MgO/NiO.

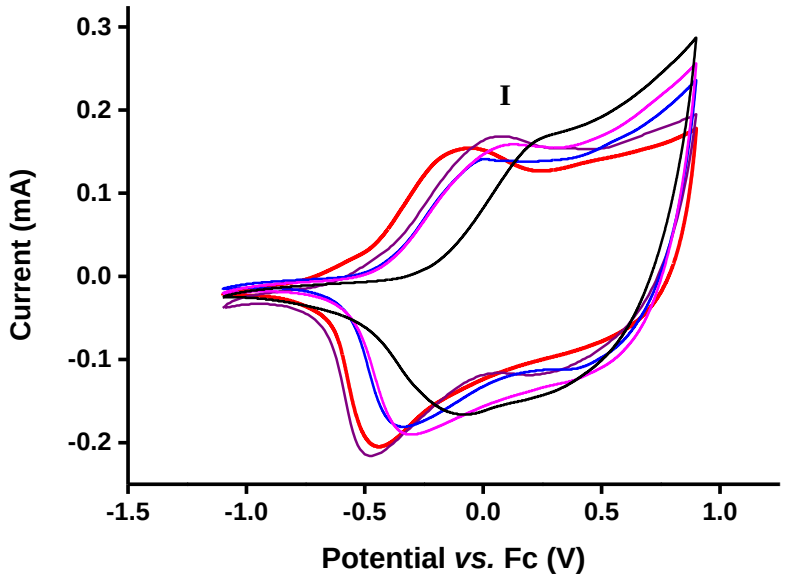

Figure 4. Cyclic voltammogram of the MgO/NiO samples recorded at a scan rate of 50 mV s^{-1} (0.1 M Li ClO_4 in CH_3CN supporting electrolyte, Pt counter electrode, recorded vs. $AgNO_3$/Ag and calibrated *vs.* $FeCp_2^+$/$FeCp_2$). Red: 0% *wt.* MgO/NiO; purple: 1% *wt.* MgO/NiO, blue: 5% *wt.* MgO/NiO; magenta: 10% *wt.* MgO/NiO; black: 25% *wt.* MgO/NiO

Electrochemical impedance spectroscopy (EIS) has been used to study the capacitive properties of the MgO/NiO mesoporous films. The measurements were carried out using a two-electrode device similar to a working p-DSC, with an undyed NiO working electrode and a Pt counter electrode combined with the iodide/triiodide redox couple. The Nyquist and Bode plots for the different MgO/NiO electrodes at a fixed bias potential are shown in Figure 5 and the plots at various applied bias potentials are shown in Figures S22-27. For the NiO-only sample at 0 V two semicircles are

observed in the Nyquist plot, the first smaller semicircle with resistance of 30 Ω and the second larger semicircle with a resistance of around 500 Ω. At higher potentials these resistances decrease and three semicircles can be seen, with the second appearing as a shoulder of the original smaller semicircle. By comparison with a platinum-platinum test measurement we have assigned the first and third semicircles as resistance at the platinum counter electrode and diffusion resistance of the electrolyte respectively, as these features are present in the test measurement with peak frequencies of 1 MHz and 5 Hz (as seen in the Bode plot, Figure S27). The second semicircle, which is not present in the test measurement, has been assigned as the resistance of the film at the NiO/electrolyte interface. This behavior agrees with that reported by D'Amario and co-workers.[4]

As the amount of Mg in the films increases this middle peak increases in size; for 0-5% *wt.* MgO/NiO the middle semicircle is only observed as a shoulder of the first and is only particularly noticeable at lower applied potentials (200-400 mV) when the film is less conductive. However for 10 and 25% *wt.* MgO/NiO this peak is visible at every applied potential, with the resistance largest for the 25% film (for these measurements the resistance at the Pt counter electrode is not visible at the chosen frequency range). For 10% *wt.* MgO at higher potentials the diffusion resistance of the electrolyte is greater than the charge transfer resistance between the electrode/electrolyte, but for 25% the dominating source of resistance is the charge transfer resistance. In the bode plots of the 10 and 25% *wt.* MgO/NiO samples the peak frequency of the diffusion resistance (around 5 Hz) remains unchanged as the applied potential increases, but the shift of the peak frequency of the charge transfer resistance as the applied potential increases is indicative of a faster interfacial reaction rate.

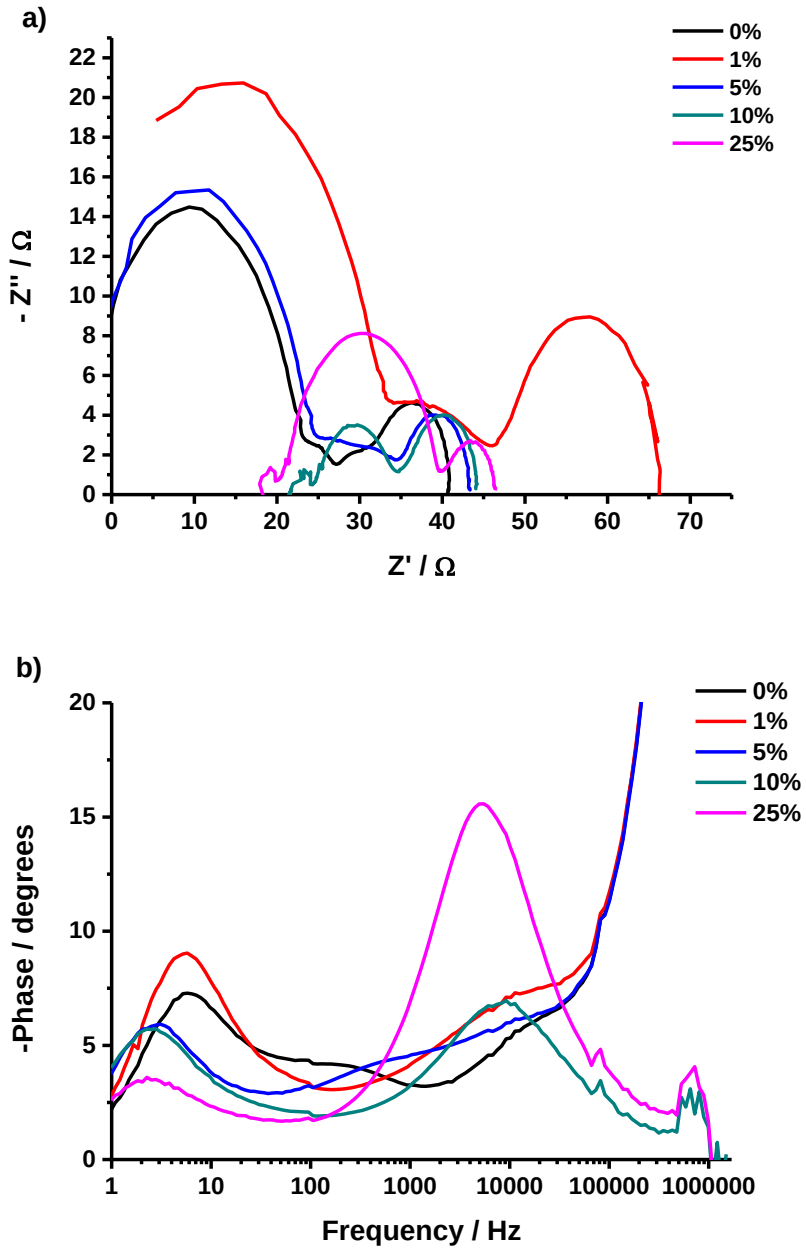

Figure 5. Overlaid Nyquist (a) and Bode (b) plots of the MgO/NiO films at an applied bias potential of 0.6 V

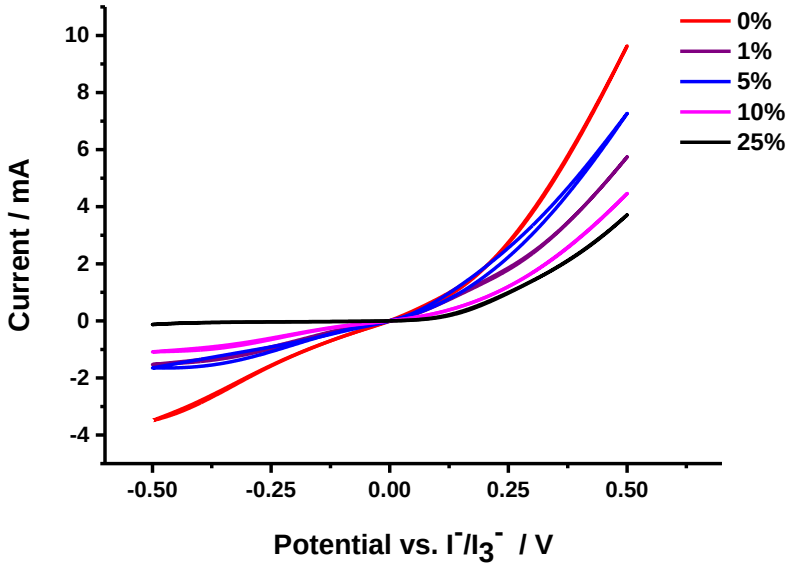

Figure 6. Cyclic voltammetry of the NiO and MgO/NiO electrodes in a two-electrode cell coupled with a platinized counter electrode in the presence of LiI/I_2 (0.1/0.1 M in 0.1M $LiClO_4$ in acetonitrile) at a scan rate of 10 mV s^{-1}. Red: 0% *wt.* MgO/NiO; purple: 1% *wt.* MgO/NiO, blue: 5% *wt.* MgO/NiO; magenta: 10% *wt.* MgO/NiO; black: 25% *wt.* MgO/NiO.

Figure 6 shows the cyclic voltammogram of the NiO and MgO/NiO electrodes in a sandwich configuration with a platinized FTO glass counter electrode, infiltrated with the redox electrolyte used in p-DSCs. The current in the positive quadrant decreases with increasing amount of MgO, suggesting the resistance for the dark reaction between the semiconductor and electrolyte increases. At reverse bias, there is a significant amount of current for the NiO device, in agreement with d'Amario *et al.*[4] This decreases with increasing concentration of MgO, until it is almost negligible for the 25% *wt.* MgO/NiO sample. This shift in the onset of the current is consistent with a shift in the valence band edge, which lies close to the redox potential of I_3^-/I^- in NiO, to more positive potentials.

Dye-sensitized solar cells

Dye Adsorption

The dye adsorption kinetics were measured by UV-visible absorption spectroscopy, with spectra taken every minute (Figure 7). The results were compared to different kinetic models, and the best fit was found for the pseudo-first order kinetic model[18], which can be explained using Equations 1 and 2.

$$q_t = q_e(1 - exp^{(-k_1 t)}) \quad (1)$$

$$ln[(q_e - q_t)/q_e] = -k_1 t \quad (2)$$

Where q_t is the adsorbed concentration of the dye at time t, q_e is the equilibrium concentration of the dye and k_1 is the pseudo-first order kinetics constant. From plotting the log term in Equation 2 versus time (Figure S4) kinetic constants were obtained. The uptake of P1 onto the NiO and MgO/NiO surfaces all displayed pseudo 1st order kinetics and the rate constants are summarized in Table S1. The rate of adsorption decreased with increasing % *wt.* of Mg. The amount of P1 adsorbed is typical for films prepared by similar methods, however the overall dye loading actually increased slightly from 0-20 % *wt.* Mg. Figure S2 shows the absorption spectra of the films used for p-DSCs.

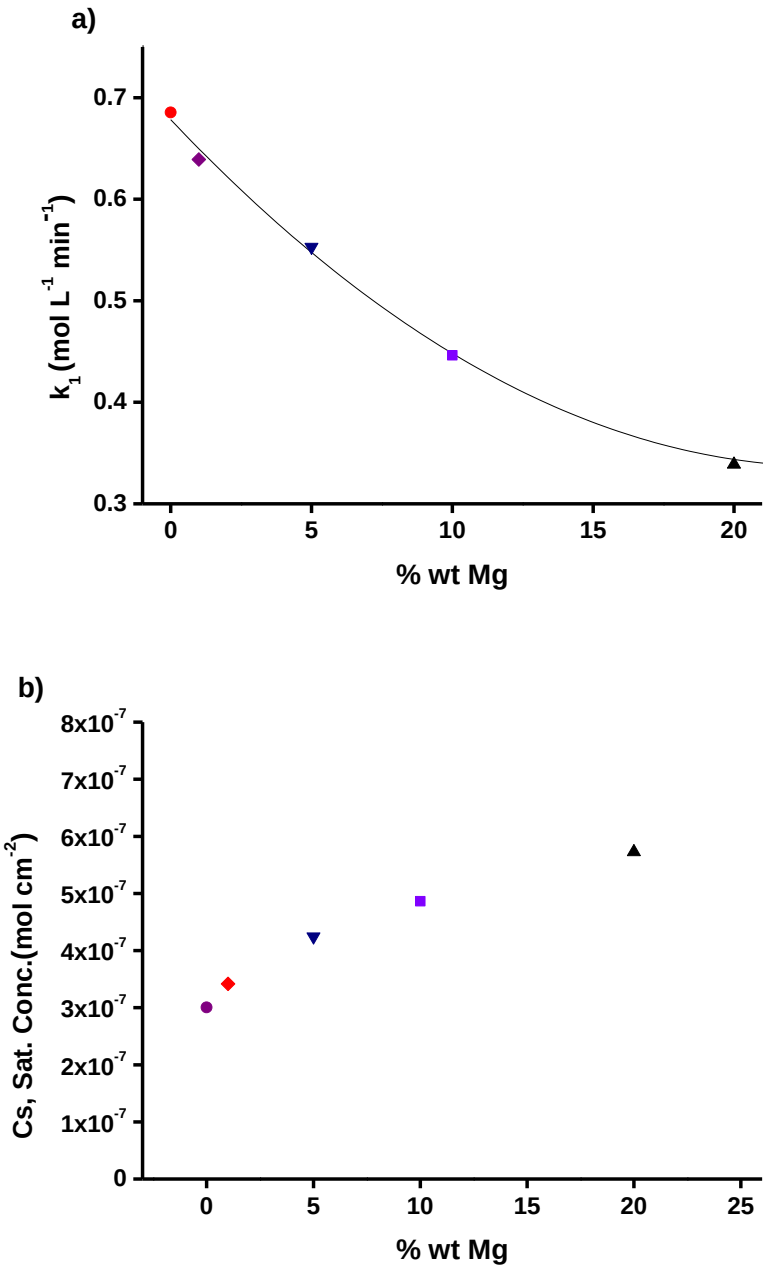

Figure 7. (a) Rate constants for adsorption of P1 onto NiO and MgO/NiO films and (b) overall dye loading concentration for the dye P1 onto NiO and MgO/NiO films.

Device performance

Table 4. Photovoltaic performance of p-DSCs based on NiO with different amounts of MgO.

% wt. $MgCl_2$	**V_{OC}[a)] [mV]**	**J_{SC}[b)] [mA cm^{-2}]**	***FF*[c)]**	**η[d)] [%]**	**IPCE[e)] [%]**
0	101	5.85	0.31	0.18	48
1	106	5.56	0.31	0.18	51
5	123	5.09	0.32	0.20	51
10	137	4.06	0.33	0.18	39
25	155	0.22	0.38	0.01	-

(a) *V*oc is the open-circuit voltage at the $J = 0$ intercept, b) *J*sc is the short-circuit current density at the $V = 0$ intercept, c) *FF* is the device fill factor; d) η is the power conversion efficiency, e) ICPE is the monochromatic incident photon-to-current conversion efficiency.

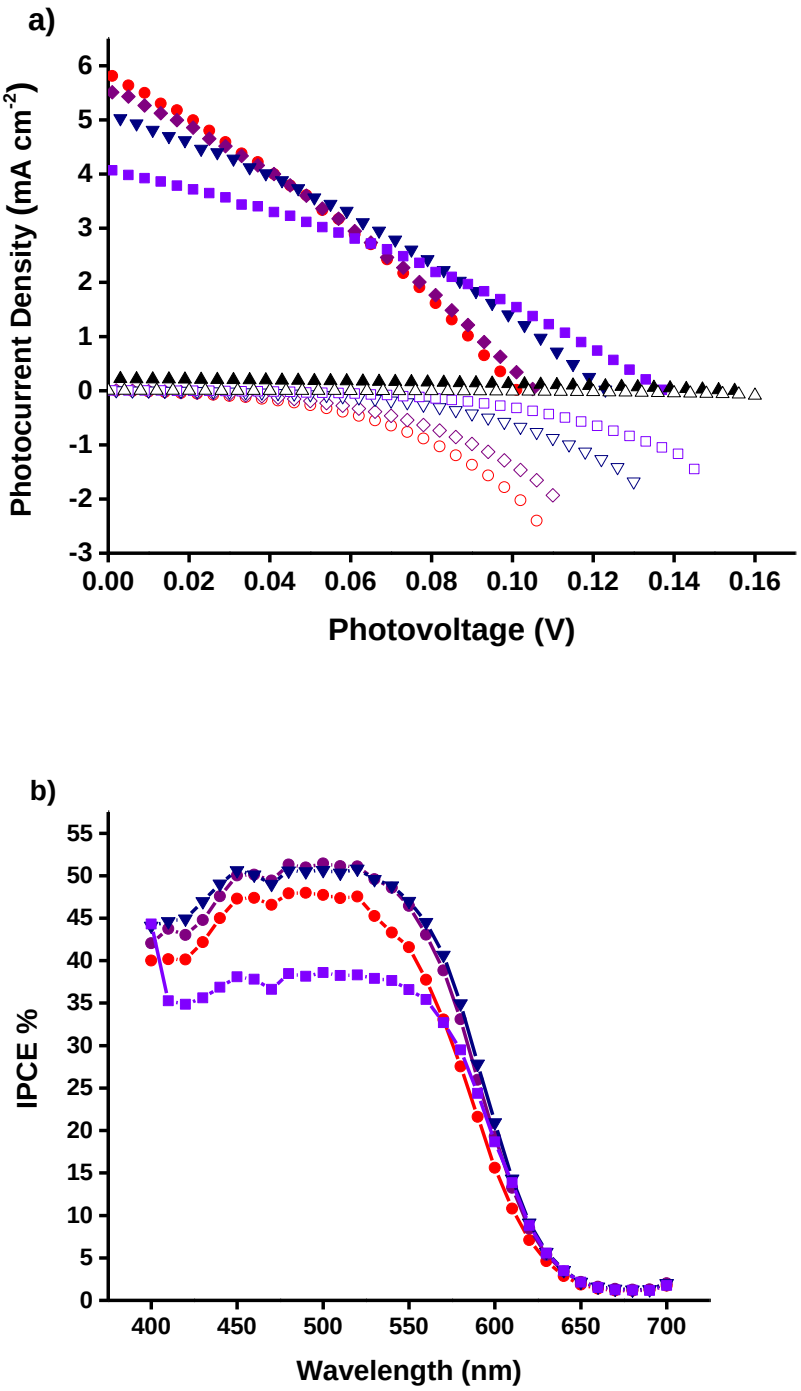

Figure 8. (a) Current-voltage curves for NiO p-type solar cells under illumination (100 mW cm^{-2}, AM1.5) (top, filled shapes) and in the dark (bottom, empty shapes) with different amounts of MgO; (b) IPCE spectra for NiO p-type solar with different amounts of MgO (0% = red circles, 1% = purple diamonds, 5% = dark blue triangles, 10% = violet squares, 25% = black triangles).

Figure 8 (a) shows the current density-photovoltage curves for the p-DSCs assembled using the NiO with 1%, 5%, 10% and 25% *wt.* MgO/NiO. In general, the photocurrent decreased and the photovoltage increased as the amount of MgO was increased. This trend in V_{OC} is consistent with the results by Huang *et al*. but in their study an optimum J_{SC} was observed for 10% *mol.* MgO.[10] The decrease in photocurrent was small for 1% and 5% MgO and the IPCE (Figure 8 (b)) for these samples was only slightly higher than those of the MgO-free sample. The photocurrent fell by 1 mA cm^{-2} and the IPCE fell by 11 % between 5% and 10% MgO and was negligible for 25% MgO. The trend in increasing V_{OC} matches the shift in the dark current curve, which could arise from the positive shift in the valence band edge brought about by doping of the material, or by a reduction in recombination at the semiconductor/electrolyte interface (*vide infra*). From Table 4 the optimum balance, and therefore efficiency, is for the 5% *wt.* MgO sample. A similar optimum Mg/NiO ratio and efficiency was observed by Huang *et al.*

Figure 9 (a) shows the charge lifetimes, which were determined by small amplitude modulated photovoltage decay experiments, plotted against V_{OC}. The equivalent time constants were shifted to higher V_{OC} with increasing % *wt*. MgO but when plotted against the charge density extracted at the equivalent V_{OC} (Q_{OC}, see Figure S30) there was only a slight increase in lifetime for the 5% and 10% *wt.* MgO/NiO electrodes compared to 0% and 1% *wt.* MgO/NiO at the equivalent Q_{OC}. The difference in lifetime cannot explain the voltage difference fully. Figure S31 shows Q_{OC} plotted against V_{OC} and the data is consistent with the positive shift in valence band edge revealed by the XPS experiments. Therefore, we attribute the general trend in Figure 9 (a) to the shift in valence band edge to positive potential, which explains the increase in photovoltage and the shift in onset potential of the dark current in Figure 8 (a).

Figure 9 (b) shows the charge transport times plotted against J_{SC}. The time constant increases with increasing % *wt.* MgO, doubling for 5% MgO/NiO compared to 0% MgO/NiO. For 25% MgO/NiO the transport time is similar to the charge lifetime in Figure 9 (b) under the conditions for the current-voltage experiments (100 mW cm^{-2}). Since the majority of charges would recombine with the electrolyte before they are extracted at the substrate, this could explain the poor efficiency of the 25% *wt*. MgO/NiO sample.

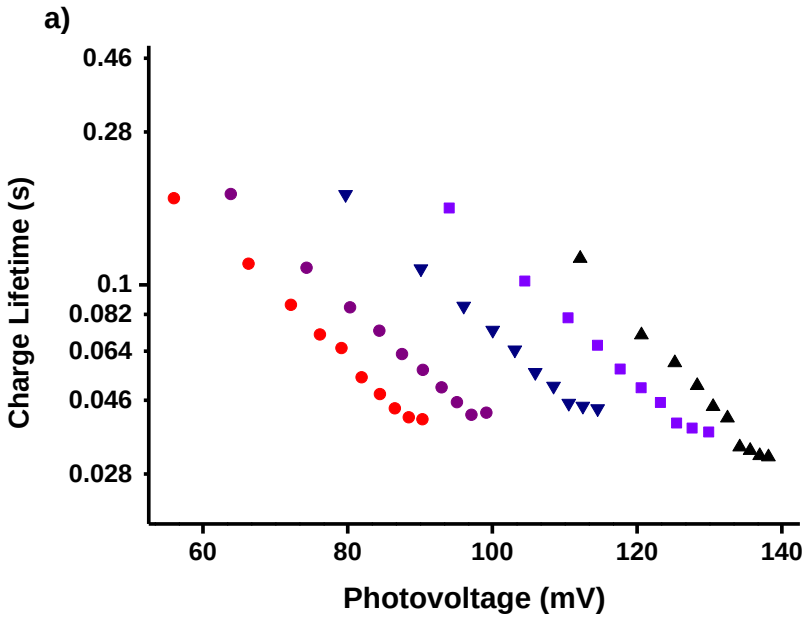

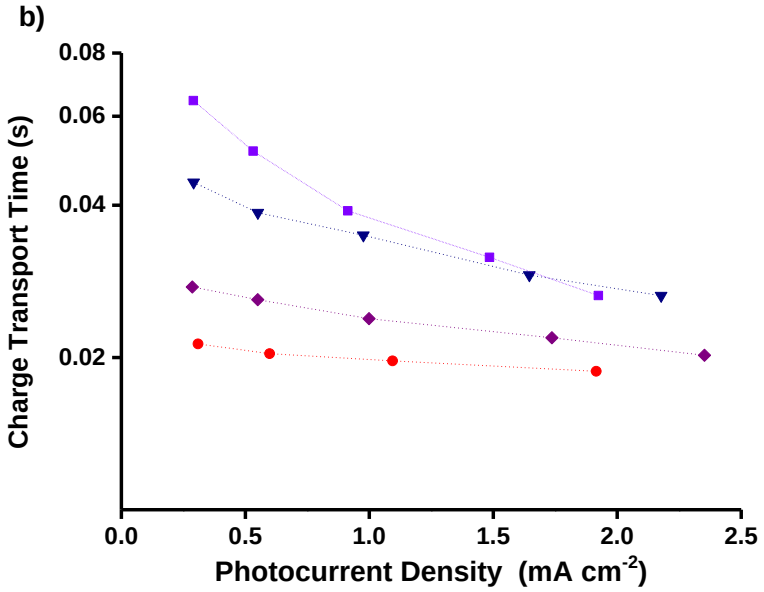

Figure 9. (a) Charge lifetime plots for NiO p-type solar cells, plotted versus photovoltage (b) Charge transport time plots for NiO p-type solar cells, plotted versus photocurrent density. Colors and symbols refer to different amounts of MgO (0% = red circles, 1% = purple diamonds, 5% = dark blue triangles, 10% = violet squares).

Discussion

Adding 1-25% *wt.* Mg to the NiO precursor solution produced solid solutions of MgO/NiO with different concentrations of Mg. The physical properties of the NiO were reasonably unchanged on addition of up to 25 *wt.* % MgO. BET adsorption isotherms show a drop in surface area with increasing MgO content, however, dye adsorption increased with increasing amount of MgO despite this. Huang *et al.* attributed this to the higher basicity of MgO compared to NiO which would favour binding though the carboxylic acid anchor. The isoelectric point of NiO is *ca.* pH 10-11, whereas the isoelectric point of MgO is pH 12.4.[19] Our studies provide an additional

explanation that the increase in the amount of dye loading is favoured by the formation of larger macropores with increasing MgO. At 10-25% *wt.* MgO all mesopores have been enveloped by macropores with 25% having the lowest BET surface area of approximately 30 $m^2 g^{-1}$.

Increasing the % *wt.* MgO shifted the current onset in the cyclic voltammetry experiments and the dark current in the p-DSCs to more positive potentials. This is consistent with a shift in valence band edge to lower energy which was observed in the XPS experiments. Deng *et al.*[20] simulated the electronic properties of solid solutions of $Mg_xNi_{1-x}O$ (where x = 0 - 1) where the valence band is shifted non-linearly with *x* until a maximum of +900 meV relative to the pure NiO valence band. According to their calculations, $x > 0.3$ is required to improve the solar cell performance and that x=0.34 used here would only shift the valence band by *ca.* 20 meV. Instead we observe experimentally a much more substantial positive shift, *ca*. 300 meV.

The IPCE is the product of the light harvesting efficiency (absorptivity) of the electrode, the charge injection efficiency and the charge collection efficiency. However, in Figure 8 the increasing dye loading is not matched by an increase in photocurrent. Instead, the J_{SC} and IPCE of the devices decreased as the % *wt.* MgO increased until no photocurrent was observed for the 25% *wt.* MgO/NiO. There could be several reasons for this. Firstly, increasing amounts of MgO could reduce the conductivity of the sample, slowing charge transport and reducing the charge collection efficiency. While the peak current appears to be the same for each sample in the cyclic voltammetry experiments, the increasing charge-transport time and decreasing dark current density with increasing % *wt.* MgO is consistent with this explanation. Secondly, charge recombination between the electrolyte and defects in the NiO could be increased by the presence of MgO, which would also limit the charge collection efficiency. The deconvolution of the Ni $2p_{3/2}$ and O 1s peaks in the XPS show an increase in the amount of Ni^{3+} species and oxygen defect sites as the doping

concentration increases. Additionally, the EIS indicated an increase in the resistance of the film at the NiO/electrolyte interface as the Mg content increased, which is consistent with increasing recombination. Only small differences in charge lifetime were observed for low Mg concentrations in our study and the work by Huang *et al.*[10] However we observed a substantially lower time constant for 25% *wt.* MgO/NiO compared to 0-10% *wt.* MgO/NiO at a similar extracted charge density. Unlike Huang *et al.* we observed an accompanying decrease in the charge transport time so for our electrodes the charge collection efficiency decreased with increasing % *wt* MgO.

The final reason for the decrease in photocurrent could be that the injection efficiency (which is dependent on the rate of photoinduced charge transfer from the NiO to the dye) must decrease with increasing % *wt.* MgO. Mori *et al.* observed that a greater driving force for charge separation between the dye and NiO is required compared to dyes adsorbed on TiO_2.[21] While Bach *et al.* reported that ca. 0.4 eV is sufficient,[22] He *et al.* proposed that more than 0.8 eV driving force for charge separation (ΔG_{inj}) is required at the NiO/dye interface.[23] The oxidation potential of P1 is 0.69 V vs. $FeCp_2^+/FeCp_2$.[24] Assuming the Fermi level in the semiconductor is close to the redox potential of process I in the cyclic voltammetry in Figure 4, ΔG_{inj} can be estimated from the average of the anodic and cathodic peaks (E'_I) using equation 3.

$$\Delta G_{inj} \approx E'_I - E'_{P1ox} \quad (3)$$

Where E'_{P1ox} is the electrochemical potential of $P1^+/P1^0$.[24]

This gives $\Delta G_{inj} \approx -0.96$ eV for NiO, $\Delta G_{inj} \approx -0.89$ eV for 5% *wt.* MgO/NiO and $\Delta G_{inj} \approx -0.66$ for 25% *wt.* MgO/NiO. We also assembled p-DSCs with C343 which has a slightly more positive redox potential than P1 ($\Delta G_{inj(C343)} \approx -0.77$ eV with 25% *wt.* MgO/NiO) but the device containing the 25% *wt.* MgO/NiO did not generate a significant photocurrent either (data not shown).

Equation 4 can be used to estimate the maximum V_{OC} from the p-DSC.

$$V_{oc} = E'_{Redox} - E_{F(NiO)} \quad (4)$$

The V_{OC} of the P1-sensitized devices in Table 4 is consistent with the quasi-Fermi level position in each material close to the redox potential of process I in Figure 4 since equation 2 predicts V_{OC} ≈ 100 mV for NiO, V_{OC} ≈ 140 mV for 5% *wt.* MgO/NiO, V_{OC} ≈ 390 V for 25% *wt.* MgO/NiO. This suggests that should a suitable sensitizer with sufficient excited state oxidizing power be used, a substantial gain in p-DSC efficiency could be achieved.

Conclusions

MgO/NiO films were prepared by the addition of increasing amounts of $MgCl_2$ to the $NiCl_2$ sol-gel solution followed by calcining in air. TEM analysis indicates that both the NiO and MgO/NiO (5%) samples are crystalline and that there was a slight increase in the overall particle size with the 5% *wt.* MgO sample. Elemental maps show an even dispersion of Mg throughout the sample. XPS analysis confirms the presence of Mg within the MgO/NiO samples and an increasing amount of Ni^{3+} with increasing Mg content. In addition, BET surface area decreased with increasing MgO concentration from approximately 41 to 30 m^2 g^{-1} as the mesopore volume decreased and macropores increased. At high concentrations between 10-25% *wt.* MgO only macropores exist indicating all mesopores have been enveloped to form macropores. The formation of larger pores could be favorable for dye diffusion and adsorption throughout the mesoporous film.

p-DSCs were constructed from the MgO/NiO films and despite the increase in dye loading with increasing MgO concentration there was a drop in the obtained photocurrent, with the 25% *wt.* MgO/NiO device producing a negligible photocurrent. This was partially attributed to a shift in the valence band to more positive potentials as the MgO content increased which resulted in an

increase in photovoltage (from the increased potential difference between the iodine/triiodide redox potential and the MgO/NiO Fermi level) but a reduction of the driving force for charge injection. Additionally, as the % *wt.* MgO was increased, a corresponding increase in the relative amount of Ni^{3+} at the surface was accompanied by a decrease in charge lifetime and an increase in transport time. This led to a decrease in charge collection efficiency and a lower IPCE with increasing Mg content. An overall increase in power conversion efficiency was obtained from the 5% *wt.* MgO/NiO. So far we have been unable to find a dye with sufficient oxidizing power to exploit the increase in voltage from the 25% *wt.* MgO/NiO electrode. These results will be used to design better dyes to work with these new electrodes to obtain a substantial increase in solar cell efficiency.

ASSOCIATED CONTENT

Supporting Information: Dye loading kinetics, BET adsorption isotherms, pXRD patterns, XPS spectra, cyclic voltammograms, EIS plots and charge lifetime data is available. This material is available free of charge via the Internet at http://pubs.acs.org.

AUTHOR INFORMATION

Corresponding Author

* †Now at the School of Chemistry, Faculty of Science, Agriculture and Engineering, Newcastle University, Newcastle upon Tyne, NE1 7RU, United Kingdom.

E-mail: elizabeth.gibson@ncl.ac.uk

Author Contributions

The manuscript was written through contributions of all authors. All authors have given approval to the final version of the manuscript.

Funding Sources

Dr Elizabeth A. Gibson -Dorothy Hodgkin Research Fellowship (Royal Society), DH100098

ACKNOWLEDGMENT

EAG thanks the Royal Society for a Dorothy Hodgkin Fellowship and the University of Nottingham for funding. TEM, EELS and EDX were obtained by Mike Fay at the Nottingham Nanoscience and Nanotechnology Centre. X-ray photoelectron spectra were obtained by Dr. Jose Portoles at the National EPSRC XPS Users' Service (NEXUS) at Newcastle University, an EPSRC Mid-Range Facility.

REFERENCES

1 Zhang, X. L.; Huang, F.; Nattestad, A.; Wang, K.; Fu, D.; Mishra, A.; Bäuerle, P.; Bach U.; Cheng, Y-B. Enhanced Open-Circuit Voltage of p-Type DSC with Highly Crystalline NiO Nanoparticles. *Chem. Commun.*, 2011, **47**, 4808–4810.

2 Bian, Z.; Tachikawa, T.; Cui, S.-C.; Fujitsuka, M.; Majima, T. Single-Molecule Charge Transfer Dynamics in Dye-Sensitized p-Type NiO Solar Cells: Influences of Insulating Al_2O_3 Layers. *Chem. Sci.*, 2012, **3**, 370-379.

3 Gibson, E. A.; Smeigh, A. L.; Le Pleux, L.; Hammarström, L.; Odobel, F.; Boschloo G.; Hagfeldt, A. Cobalt Polypyridyl-Based Electrolytes for p-Type Dye-Sensitized Solar Cells. *J. Phys. Chem. C*, 2011, **115**, 9772–9779.

4 D'Amario, L.; Boschloo, G.; Hagfeldt A.; Hammarström, L. Tuning of Conductivity and Density of States of NiO Mesoporous Films used in p-Type DSSCs. *J. Phys. Chem. C*, 2014, **118**, 19556–19564.

5 Natu, G.; Hasin, P.; Huang, Z.; Ji, Z.; He, M.; Wu, Y. Valence Band-Edge Engineering of Nickel Oxide Nanoparticles via Cobalt Doping for Application in p-Type Dye-Sensitized Solar Cells. *ACS Appl. Mater. Interfaces*, 2012, **4**, 5922–5929.

6 Renaud, A.; Cario, L.; Deniard, P.; Gautron, E.; Rocquefelte, X.; Pellegrin, Y.; Blart, E.; Odobel, F.; Jobic, S. Impact of Mg Doping on Performances of $CuGaO_2$ Based p-Type Dye-Sensitized Solar Cells. *J. Phys. Chem. C*, 2014, **118**, 54–59.

7 Xiong, D.; Zhang, W.; Zeng, X.; Xu, Z.; Chen, W.; Cui, J.; Wang, M.; Sun, L.; Cheng, Y.B. Enhanced Performance of p-Type Dye-Sensitized Solar Cells Based on Ultrasmall Mg-Doped $CuCrO_2$ Nanocrystals. *ChemSusChem*, 2013, **6**, 1432–1437.

8 Taurian, O. E.; Springborg, M.; Christensen, N. E. Self-Consistent Electronic Structures of MgO and SrO. *Solid State Commun.*, 1985, **55**, 351–355.

9 Fujimori, A.; Minami, F. Valence-Band Photoemission and Optical Absorption in Nickel Compounds. *Phys. Rev. B*, 1984, **30**, 957–971.

10 Huang, Z.; Zeng, X.; Wang, H.; Zhang, W.; Li, Y.; Wang, M.; Cheng Y-B.; Chen, W. Enhanced Performance of p-Type Dye Sensitized Solar Cells Based on Mesoporous $Ni_{1-x}Mg_xO$ Ternary Oxide Films. *RSC Adv.*, 2014, **4**, 60670–60674.

11 Sumikura, S.; Mori, S.; Shimizu, S.; Usami, H.; Suzuki, E. Syntheses of NiO Nanoporous Films Using Nonionic Triblock Co-Polymer Templates and Their Application to Photo-Cathodes of p-Type Dye-Sensitized Solar Cells. *J. Photochem. Photobiol., A*, 2008, **199**, 1–7.

12 Li, L.; Gibson, E. A.; Qin, P.; Boschloo, G.; Gorlov, M.; Hagfeldt A.; Sun, L. Double-Layered NiO Photocathodes for p-Type DSSCs With Record IPCE. *Adv. Mater.*, 2010, **22**, 1759–1762.

13 Duffy, N.; Peter, L.; Rajapakse R. M.; Wijayantha, K. G.; A Novel Charge Extraction Method for the Study of Electron Transport and Interfacial Transfer in Dye Sensitised Nanocrystalline Solar Cells. *Electrochem. Commun.*, 2000, **2**, 658–662.

14 Ahn, C. C.; Krivanek, O. L. *EELS Atlas : A Reference Collection of Electron Energy Loss Spectra Covering All Stable Elements*, Gatan.Inc, 1983.

15 Zhao, B.; Ke, X. K.; Bao, J. H.; Wang, C. L.; Dong, L.; Chen, Y. W.; Chen, H. L. Synthesis of Flower-Like NiO and Effects of Morphology on its Catalytic Properties. *J. Phys. Chem. C*, 2009, **113**, 14440–14447.

16 Boschloo, G.; Hagfeldt, A. Spectroelectrochemistry of Nanostructured NiO. *J. Phys. Chem. B*, 2001, 105, 3039-3044

17 Awais, M.; Dowling, D. D.; Rahman, M.; Vos, J. G.; Decker, F.; Dini, D. Spray-Deposited NiOx films on ITO substrates as photoactive electrodes for p-type dye-sensitized solar cells. *J. Appl. Electrochem*, 2013, **43**, 191-197

18 Giovannetti, R.; Zannotti, M.; Alibabaei, L.; Ferraro, S. Equilibrium and Kinetic Aspects in the Sensitization of Monolayer Transparent TiO_2 Thin Films with Porphyrin Dyes for DSSC Applications. *Int. J. Photoenergy*, 2014, **2014**, 1–9.

19 Parks, G. A. The Isoelectric Points of Solid Oxides, Solid Hydroxides and Aqueous Hydroxo Complex Systems. *Chem. Rev.*, 1965, **65**, 177–198.

20 Deng, J.; Mortazavi, M.; Medhekar, N. V.; Zhe Liu, J. Band Engineering of $Ni_{1-x}Mg_xO$ Alloys for Photocathodes of High Efficiency Dye-Sensitized Solar Cells. *J. App. Phys.*, 2012, **112**, 123703.

21 Mori, S.; Fukuda, S.; Sumikura, S.; Takeda, Y.; Tamaki, Y.; Suzuki, E.; Abe, T. Charge-Transfer Processes in Dye-Sensitized NiO Solar Cells. *J. Phys. Chem. C*, 2008, **112**, 16134–16139.

22 Powar, S.; Xiong, D.; Daeneke, T.; Ma, M. T.; Gupta, A.; Lee, G.; Makuta, S.; Tachibana, Y.; Chen, W.; Spiccia, L.; Cheng, Y.; Götz, G.; Bäuerle P.; Bach, U. Improved Photovoltages for p-Type Dye-Sensitized Solar Cells Using $CuCrO_2$ Nanoparticles. *J. Phys. Chem. C*, 2014, **118**, 16375–16379.

23 Liu, Z.; Xiong, D.; Xu, X.; Arooj, Q.; Wang, H.; Yin, L.; Li, W.; Wu, H.; Zhao, Z.; Chen, W.; Wang, M.; Wang.; Cheng, Y.-B.; He, H. Fine Tuning of Fluorene-Based Dye Structures for High-Efficiency p-Type Dye-Sensitized Solar Cells. *ACS Appl. Mater. Interfaces.*, 2014, **6**, 3448–3454.

24 Qin, P.; Wiberg, J.; Gibson, E. A.; Linder, M.; Li, L.; Brinck, T.; Hagfeldt, A.; Albinsson, B.; Sun, L. Synthesis and Mechanistic Studies of Organic Chromophores with Different Energy Levels for p-Type Dye-Sensitized Solar Cells. *J. Phys. Chem. C*, 2010, **114**, 4738–4748.

Table of Contents Graphic